Journal of Heat and Mass Transfer Research

Journal homepage: https://jhmtr.semnan.ac.ir

Semnan University

ISSN: 2383-3068

Research Article

Analysis of Mixed Convection inside an Enclosure in the Presence of a Rotating Grooved Cylinder

Rahim Hassanzadeh [a]*, Reza Rahimi [a], Vahideh Rahimi Hajifirouzi [b]

[a] *Faculty of Mechanical Engineering, Urmia University of Technology, Urmia, Iran*

[b] *Department of Engineering, Ahar Branch, Islamic Azad University, Ahar, Iran*

ARTICLE INFO

Article history:

Received: 2023-01-21

Revised: 2024-03-06

Accepted: 2024-03-09

Keywords:

Grooved cylinder;

Heat transfer enhancement;

Mixed convection;

Rotating cylinder.

ABSTRACT

In the present study, mixed convective heat transfer inside a square enclosure in the presence of a rotating cylinder with various numbers of grooves is presented. Effects of counterclockwise and clockwise rotations with non-dimensional rotating speeds (RS) in the range from -1000 to 1000 are studied for different radius ratios (R) of 0.1, 0.2, and 0.3. Computations are carried out for Rayleigh numbers 103, 104, and 105 using the finite volume approach. The obtained results are validated against the available data for an empty enclosure (in the absence of a cylinder) as the reference case and also for an enclosure with a rotating smooth cylinder. It is demonstrated that for a specific value of the Rayleigh number, increasing the radius ratio enhances the thermal performance inside the enclosure regardless of the groove number and rotating speed. Increasing the Rayleigh number attenuates the roles of rotating speed and radius ratio, gradually. It is concluded that among all cases, the case with counterclockwise rotating smooth cylinder and among the grooved cases, Case 5 with three grooves provide the maximum heat transfer enhancements.

1. Introduction

The natural convection inside an enclosure has been the topic of many investigations over the recent decades due to numerous engineering applications. On the other hand, heat and fluid flow around a rotating cylinder has attracted the attention of researchers because of its significant role in industry and engineering fields.

Recently, the investigators have paid a great abundance of attention to the natural and mixed convective heat transfer inside an enclosure containing phase change material [1-7]. Selimefendigil and Öztop [1] studied the effect of a rotating cylinder on mixed convection of a differentially heated cavity filled with a phase change material. They investigated the impact of different parameters including angular rotating speed, location, and size of the cylinder on heat and fluid flow, and stated that the heat transfer and melting process can be controlled by utilizing a rotating cylinder inside the cavity. In another numerical work, Ouri et al. [8] explored the magneto-hydrodynamic convection and phase change process of a vented cavity with L-shaped geometry equipped with an inner rotating cylinder and phase change material–packed bed system. Considering various values of the Reynolds number, rotational Reynolds number, the radius of the cylinder, and Hartmann number, the authors reported that recirculation regions inside the cavity can be controlled by the varying radius of the cylinder and rotational Reynolds number along with the magnetic field.

* **Corresponding author.**
E-mail address: r.hassanzadeh@uut.ac.ir

Cite this article as:
Hassanzadeh, R., Rahimi, R. and Rahimi Hajifirouzi, V., 2024. Analysis of Mixed Convection inside an Enclosure in the Presence of a Rotating Grooved Cylinder. *Journal of Heat and Mass Transfer Research*, 11(1), pp. 61-74.
https://doi.org/10.22075/JHMTR.2024.29691.1415

Several researchers have addressed the natural and mixed convection problems within a differentially heated cavity [1, 9-12]. For instance, the natural convection of a square cavity with a non-uniformly heated wall on the left side, and a uniformly cooled wall on the right side was studied by Turkyilmazoglu [13]. Presenting a visual analysis of heat transport and mixing due to natural convection, the author illustrated that redistribution of streamlines and temperatures takes place as a result of non-uniform surface heating, and concluded that the best heat transfer rate can be reached in a case in which heating source is positioned near the top adiabatic wall. Hassanzadeh et al. [10] investigated the impact of a rotating rough cylinder located inside a differentially heated square enclosure on the natural convective heat transfer. They studied the effect of various parameters including the number of roughness components, Rayleigh number, radius ratio, non-dimensional rotating speed, and rotation direction. According to their results, the maximum heat transfer enhancement as a consequence of cylinder rotation occurred in the case with a smooth cylinder under the lowest Rayleigh number, the largest cylinder size, and the highest clockwise rotating speed. In order to analyze the thermomagnetic performance of an inclined partially porous enclosure with discrete hot and cold walls, a numerical investigation has been conducted [14]. The author stated that by placing the hot wall close to the bottom, Nusselt number could increase in general. In addition, an increase in the thickness of the porous media at the inclination angle of 30 degrees was reported to increase the Nusselt number by 52%. Another study analyzed the buoyancy driven heat transfer of Cu-water nanofluid in a differentially heated cavity with an inner adiabatic square baffle considering the influence of different parameters such as the Rayleigh number, baffle position, and volume fraction of nanoparticles [15]. The results indicated that higher Rayleigh numbers and volume fraction of nanoparticles led to enhanced heat transfer rate. Mixed convection of Al_2O_3-water nanofluid within a lid-driven cavity with differentially heated walls was studied by Hemmat Esfe and Saedodin [16]. Exploring various slopes of the cavity under different Richardson numbers, the authors pointed out that the convective heat transfer rate decreases with increasing inclination angle to 90 degrees.

The geometry of cavities plays a key role in the thermal analysis of investigated problems. In this line, researchers have analyzed natural and mixed convection inside enclosures with various geometries such as grooved [4], L-shaped [8], elliptical [17], F-shaped [18], and cylindrical [19, 20] cavities. Additionally, the impact of utilizing rotating cylinders inside an enclosure on heat and fluid flow has led researchers to concentrate on analyzing it under different scenarios. For instance, some researchers studied the impact of rotating cylinders in lid-driven cavities [21-23]. Barnoon et al. [21] studied the mixed convection and entropy generation inside a square enclosure with nanofluid under a magnetic field effect. Moayedi et al. [22] investigated the impact of fin shape on mixed convection inside a lid-driven square enclosure. Triveni and Panua [23] conducted a numerical study to analyze the natural and mixed convection of a cavity filled with nanofluid in the presence of heated cylinders. Some researchers have addressed the heat transfer of an enclosure with porous media in their research [2, 24-27]. Tahmasbi et al. [24] investigated the mixed convection inside a square enclosure with optimized porous media and nanofluid in the presence of two rotating cylinders. Aly et al. [25] studied the natural convection flow of a horizontal wavy cavity filled with nanofluid under the effect of rotating cylinders. Jabbar et al. [27] carried out an investigation around the convective heat transfer inside an enclosure with porous media filled with copper-water nanofluid in the presence of a rotating cylinder.

Some researchers studied various topics including a grooved cylinder in order to achieve different goals [28-35]. Song et al. [34] numerically investigated the impact of geometrical parameters on the drag reduction of a triangular grooved cylinder by means of response surface methodology. Wang et al. [35] conducted an experimental study to examine the global aerodynamic forces of a cactus-shaped rigid cylinder with a constant groove depth-to-diameter ratio. Derakhshandeh and Gharib [30] analyzed the instabilities of laminar flow around a grooved cylinder with three various groove geometry. Fujisawa et al. [32] experimentally studied the effect of grooves located on the surface of a circular cylinder on aerodynamic noise reduction. Caliskan et al. [29] conducted experiments using Particle Image Velocimetry (PIV) to investigate the flow behavior around grooved and smooth cylinders located in shallow water. Derakhshandeh et al. [36] examined heat and fluid flow around a grooved cylinder with different groove types and groove positions. Ozalp et al. [33] experimentally studied the thermal-hydraulic effect of utilizing a grooved cylinder as a control cylinder upstream of a bare cylinder. Afroz and Sharif [28] carried out numerical simulations to study the flow over a grooved cylinder at low Reynolds numbers.

Among all that being said, the mixed convection of a cavity containing a rotating grooved cylinder has not yet been studied

according to the author's knowledge. The existence of a number of grooves on a rotating cylinder inside an enclosure can affect the heat transfer process of the cavity flow, which is not investigated before. Hence, this investigation presents numerical results around this subject studying the effect of different parameters including Rayleigh number, cylinder radius ratio, number of grooves on the cylinder, and non-dimensional rotating speed.

2. Problem Definition and Modeling

In this study, the laminar two-dimensional mixed convection inside a square enclosure containing a rotating grooved cylinder is conducted by means of the finite-volume method. Fig. 1 illustrates the schematic of the studied cases in this investigation. In order to estimate the thermal performance of utilizing rotating grooved cylinders within the enclosure, Case 1 has been defined as the reference case, which is a differentially heated cavity without a cylinder. Among the other cases, Case 2 contains a smooth cylinder in the center of the enclosure, and Cases 3-6 include a grooved cylinder with one, two, three, and four grooves, respectively.

Fig. 2 shows the geometrical details of the two-dimensional computational domain. The width and height of the enclosure are L×L and the radius of the cylinder is r. The dimensions of grooves are defined as w×w, where w=0.1d. Three different radius ratios are defined for the rotating cylinder including R=0.1, 0.2, and 0.3, which has been studied for all Cases 2-6. Non-dimensional rotating speeds of RS=100, 500, and 1000 have been considered for counterclockwise rotation, and RS=-100, -500, and -1000 for clockwise rotation of the cylinder. Also, the impact of using stationary grooved cylinders has been analyzed, i.e. RS=0. In addition, Rayleigh numbers 10^3, 10^4, and 10^5 are studied for all under consideration cases.

The variations of the Richardson number for all cases are shown in Fig. 3 as a function of the Rayleigh number and rotating speed. This figure provides additional information regarding the values of the Richardson number, as the criterion for mixed convection, at all RS and R values to show that the mixed convection occurs inside the enclosure. Here, the values of the Richardson number change between 0.1 and 10^6.

The fluid properties of water with a Prandtl number of 7.0 is set to be constant at bulk temperature except for density, which linearly varies as a function of temperature based on the Boussinesq approximation.

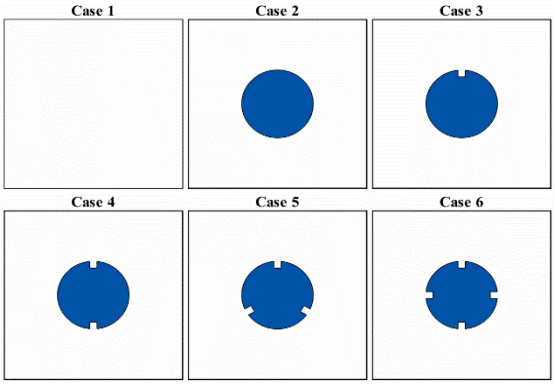

Fig. 1. Schematic of under consideration cases;
Case 1: cavity without a cylinder (Ref. case);
Case 2: cavity with a smooth circular cylinder;
Case 3: cavity with a cylinder having one square groove;
Case 4: cavity with a cylinder having two square grooves;
Case 5: cavity with a cylinder having three square grooves;
Case 6: cavity with a cylinder having four square grooves

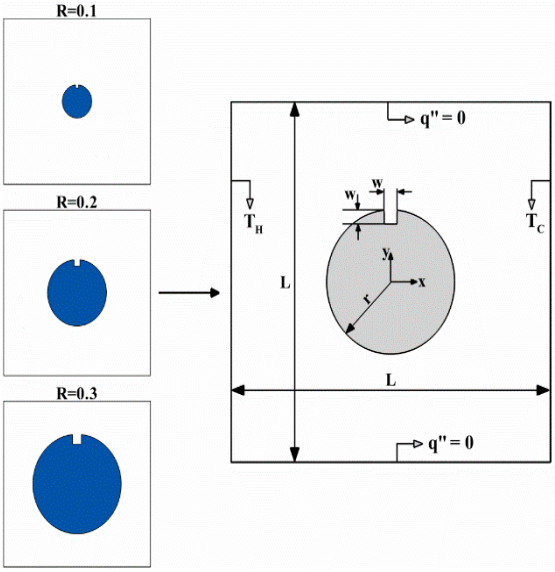

Fig. 2. Computational flow domain applied in the present study

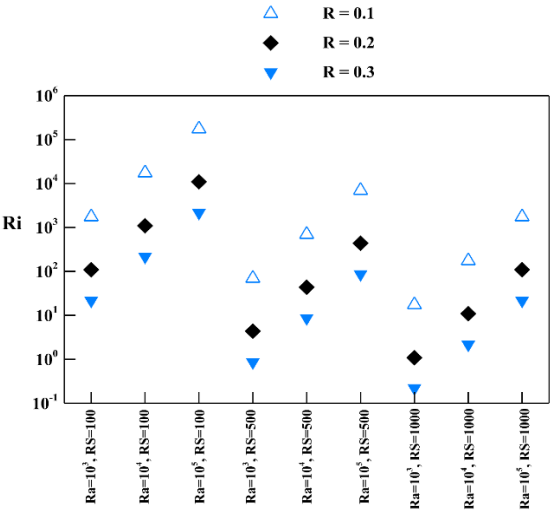

Fig. 3. Variations of the Richardson number for different radius ratios as a function of RS and Ra

The governing equations for laminar, steady, two-dimensional, and incompressible flow are as follows;

$$\frac{\partial u}{\partial x}+\frac{\partial v}{\partial y}=0 \tag{1}$$

$$u\frac{\partial u}{\partial x}+v\frac{\partial u}{\partial y}=-\frac{1}{\rho}\frac{\partial p}{\partial x}+\vartheta\left(\frac{\partial^2 u}{\partial x^2}+\frac{\partial^2 u}{\partial y^2}\right) \tag{2}$$

$$u\frac{\partial v}{\partial x}+v\frac{\partial v}{\partial y}=-\frac{1}{\rho}\frac{\partial p}{\partial y}+\vartheta\left(\frac{\partial^2 v}{\partial x^2}+\frac{\partial^2 v}{\partial y^2}\right)+g\beta(T-T_{ref}) \tag{3}$$

$$u\frac{\partial T}{\partial x}+v\frac{\partial T}{\partial y}=\alpha\left(\frac{\partial^2 T}{\partial x^2}+\frac{\partial^2 T}{\partial y^2}\right) \tag{4}$$

Equations (1-4) represent continuity, x-momentum, y-momentum, and energy equations, respectively. In order to compute the governing equations numerically, a finite-volume code has been utilized. The second-order upwind scheme is used to discretize all advection and convective terms, and the central differencing scheme is used for the discretization of diffusion terms. The pressure term is discretized using the body-forced weighted scheme, and velocity and pressure fields are coupled using the SIMPLE algorithm [37]. The convergence criterion of 10^{-7} is set for all equations. The following boundary conditions are used to solve the resultant discretized equations;

On the surface of the cylinder (for counterclockwise rotation):

$$\begin{aligned} u &= -\frac{d}{2}\omega\cdot RS\cdot\sin(\varphi)\\ v &= \frac{d}{2}\omega\cdot RS\cdot\cos(\varphi)\\ \left.\frac{\partial T}{\partial r}\right|_{r=d/2} &= 0 \end{aligned} \tag{5}$$

On the surface of the cylinder (for clockwise rotation):

$$\begin{aligned} u &= \frac{d}{2}\omega\cdot RS\cdot\sin(\varphi)\\ v &= -\frac{d}{2}\omega\cdot RS\cdot\cos(\varphi)\\ \left.\frac{\partial T}{\partial r}\right|_{r=d/2} &= 0 \end{aligned} \tag{6}$$

On the right wall of the enclosure:

$$\begin{aligned} u &= v = 0\\ T &= T_C \end{aligned} \tag{7}$$

On the left wall of the enclosure:

$$\begin{aligned} u &= v = 0\\ T &= T_H \end{aligned} \tag{8}$$

On the upper and lower wall of the enclosure:

$$\begin{aligned} u &= v = 0\\ \frac{\partial T}{\partial y} &= 0 \end{aligned} \tag{9}$$

Additionally, the following non-dimensional variables are used in the present work:

$$Ra=\frac{g\beta(T_H-T_C)L^3}{\vartheta\alpha} \tag{10}$$

$$Ri=\frac{Ra}{Re^2Pr} \tag{11}$$

$$RS=\frac{\omega L^2}{\alpha} \tag{12}$$

$$Re=\frac{(r\omega)L}{\vartheta} \tag{13}$$

$$R=\frac{r}{L} \tag{14}$$

$$\theta=\frac{T-T_C}{T_H-T_C} \tag{15}$$

$$Pr=\frac{\vartheta}{\alpha} \tag{16}$$

The Nusselt number is obtained using the following equation:

$$Nu=\frac{1}{L}\int_{-L/2}^{L/2}Nu_y dy \tag{17}$$

3. Grid Size Independence Study

A quad-type grid distribution is generated in the present investigation, which is shown in Fig. 4. To assess the verification of the computational grids, a grid size independence study is carried out in this section. Eight different grids with a non-dimensional element size of ξ/d between 0.010 and 0.075 are studied for Case 3 under RS=500, R=0.2, and Ra=104, which results in grids with cell numbers 1028, 2237, 3503, 6144, 8704, 13915, 24795, and 55294.

The details of under consideration grids are presented in table 1.

The computed results of the grid size independence study are shown in Fig. 5. As indicated, the deviation for the average Nusselt number between Grid 5 and Grid 6 is less than 0.50%. Thus, the grid details of Grid 5 with ξ/d=0.025 is chosen to apply to other cases in this study.

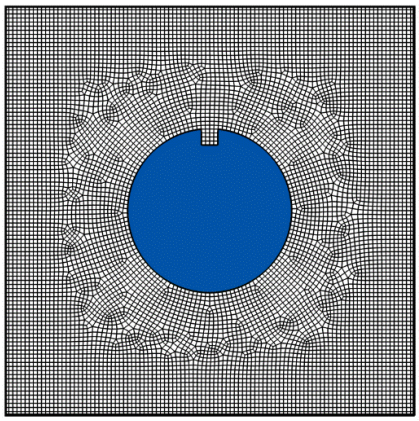

Fig. 4. Grid distribution within the flow domain

Table 1. Details of tested grids for grid size independence study

Grid No.	ξ/d	Cell number
1	0.075	1028
2	0.050	2237
3	0.040	3503
4	0.030	6144
5	0.025	8704
6	0.020	13915
7	0.015	24795
8	0.010	55294

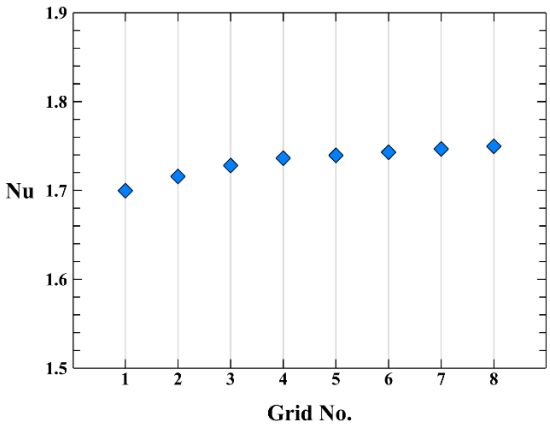

Fig. 5. Results of grid size independence study

4. Validation Study

In this section, the results of the validation study are presented to check the validity of the applied code. The validation study is done in two steps: i) Case 2 under RS=100, Ra=10^5, and R=0.2 regarding the average Nusselt number and isotherm patterns against available data by Roslan et al. [38], ii) Case 1 under Ra=10^4 and 10^5 regarding average Nusselt number against the available data by Roslan et al. [38], Khanafer et al. [39], and Ho et al. [40]. The results of the first step are shown in Fig. 6, and the results of the second step are presented in Table 2. Comparing the obtained results with available data confirms the accuracy of the applied code in the present study.

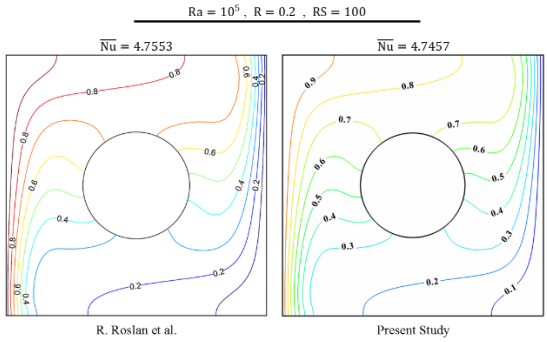

Fig. 6. Validation of applied code against the available data [38] for Case 2 under R=0.2, RS=100, and Ra=10^5

Table 2. Validation of numerical code against the available data for Case1

Ra	Nu			
	Roslan et al. [38]	Khanafer et al. [39]	Ho et al. [40]	Present study
Ra=10^4	2.272	2.299	2.297	2.262
Ra=10^5	4.176	4.720	4.552	4.693

5. Results and Discussion

The computed results are reported as both quantitative and qualitative results and compared with each other in this section. The effect of all under consideration parameters including radius ratio, rotating speed, the direction of rotation, and Rayleigh number are discussed using a number of figures. Finally, the thermal performance of each simulation is presented to discuss the overall performance of utilizing a grooved cylinder with different numbers of grooves inside a differentially heated enclosure.

5.1. Effects of Radius Ratio

Fig. 7 indicates the impact of the non-dimensional radius ratio on the streamlines pattern within the enclosure with smooth and grooved cylinders under RS=1000, Ra=10^4, and R=0.1, 0.2, and 0.3. As it seems, the dimensionless radius ratio plays an important role in the formation of vortices inside the enclosure. The flow structure is more complex in the smallest radius ratio (R=0.1) compared to other larger radius ratios. In this radius ratio, regardless of the groove number, the shear-driven flow is close to the cylinder and a considerable buoyancy-driven flow has occupied a large area at the far field of the cylinder. For a smooth cylinder (Case 2), four vortical structures develop on the upper and lower shoulders of the cylinder called corner vortices. In Case 3 and Case 4, the formed vortices show a tendency to merge with each other at the left and right sides of the cylinder. In Case 5, as demonstrated, the lower vortices completely

merge with each other and occupy the lower surface of the grooved cylinder and the upper vortices expand gradually. In the last case with four grooves (Case 6), four distinguishable larger-scale vortices observe on the upper and lower shoulders of the cylinder. Increasing the radius ratio up to 0.2 expands the occupied region by counterclockwise rotating shear-driven flow and restricts the buoyancy flow at the corners of the enclosure. It is due to an increase in the cylinder surface area, which provides more shear-driven flow. Therefore, the interaction between two counter-rotating shear-driven and buoyancy-driven zones develops four vortical structures at the corners of the enclosure. On the other hand, an examination of the presented streamline patterns shows that the smooth cylinder forms a stronger shear-driven flow inside the enclosure in comparison to the grooved cylinders. Due to this occurrence, the corner vortices are relatively larger for grooved cases compared to the case with a smooth cylinder. In the largest radius ratio of 0.3, the occupied region by shear-driven flow expands more and more for all cases due to an additional increase in the cylinder surface area, and the corner vortices shrink correspondingly as illustrated in Fig. 7. Like as the R=0.2, for R=0.3, the resultant shear-driven flow is stronger for the smooth cylinder case than all grooved cases.

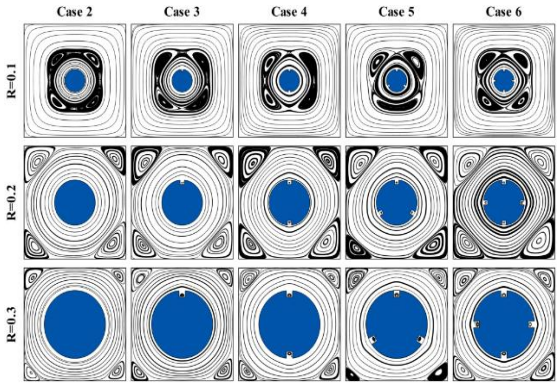

Fig. 7. Effect of radius ratio on the streamline patterns for RS=100 and Ra=10^4

Fig. 8 is presented to illustrate the impact of the radius ratio on the non-dimensional velocity distribution along the vertical line near the left wall (x/L=-0.4) for Ra=10^4, RS=100, and R=0.1, 0.2, and 0.3. Here, the velocity magnitudes are normalized using the tangential velocity of the cylinder. As demonstrated, in the R=0.1, no considerable differences can be seen among the cases since this vertical line (x/L=-0.4) passes from the buoyancy-driven flow for all cases. With an increase in the radius ratio up to 0.2, the velocity magnitude reduces for all cases and the difference among the cases appears. For |y|>0.25, the velocity fields are quite low for all cases, and for |y|<0.25, the velocity magnitudes augment suddenly and form a peak point around the mid location. Around the maximum peak point, the velocity magnitudes are higher for Case 2 having the smooth cylinder compared with grooved cases. This occurrence is due to this fact that the smooth cylinder develops higher amount of the shear-driven flow than the other cases as discussed before. With increasing the radius ratio up to 0.3, the velocity magnitudes augment considerably for all cases and the difference among the cases becomes more evident. Except around the peak point, the maximum and minimum near-wall velocity can be reported for Case 5 and Case 6, respectively. In addition, due to expanding the shear-driven flow, the occupied region with low-velocity fields reduces close to upper and lower insulated walls, and further shrinking of corner vortices as a result of an additional shear-driven flow occurs.

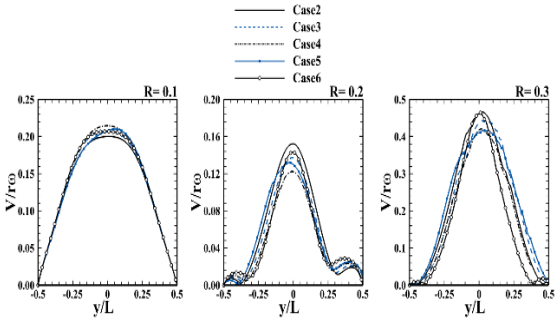

Fig. 8. Effect of radius ratio on the non-dimensional velocity magnitude at x/L=-0.4 for RS=100 and Ra=10^4

In order to gain a better understanding of the effect of radius ratio on near-wall (x/L=-0.4) non-dimensional temperature distribution, Fig. 9 is presented for Ra=10^4, RS=100, and R=0.1, 0.2, and 0.3. In the case with a minimum radius ratio of 0.1, more or less, similar temperature distributions can be seen for all cases due to nearly the same velocity magnitudes as discussed before. In this radius ratio, the near-wall temperature augments gradually from the lower insulated wall toward the upper wall. Increasing the radius ratio up to 0.2 increases the near-wall temperature gradient for Case 2 more than the other cases. This event is because of the stronger shear-driven flow and consequently higher velocity gradient developed by Case 2 as discussed before. Among the grooved cylinder cases, it seems Case 6 has the maximum temperature distribution and minimum temperature gradient. For the radius ratio of 0.3, at most locations, Case 2 and Case 6 provide the maximum and minimum temperature gradients, respectively. However, at some restricted points close to the upper wall, Case 5 develops the maximum temperature gradient having the maximum velocity gradient at these points.

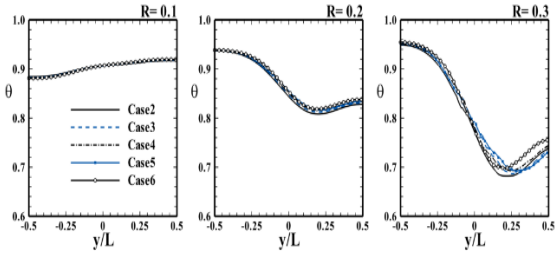

Fig. 9. Effect of radius ratio on the non-dimensional temperature at x/L=-0.4 for RS=100 and Ra=10^4

5.2. Effects of Rotating Speed

Another issue, regarding the rotation of smooth and grooved cylinders inside a differentially heated enclosure, is the non-dimensional rotating speed, which is studied in this subsection.

Fig. 10 illustrates the effect of different non-dimensional counterclockwise rotating speeds on flow patterns inside the enclosure under Ra=10^4 and R=0.2. For all stationary cases, i.e. RS=0, the heated fluid moves upward along the left wall and moves horizontally from left to right along the upper insulated wall. Since the right wall is defined as a cold wall, the heated fluid loses a portion of its heat to the right wall by being in the vicinity of the cold wall and consequently moves downward along this wall, and then the colder fluid elements move from right to left along the lower insulated wall. Thus, a clockwise buoyancy-driven fluid flow dominates in the free space between the cylinder and enclosure walls regardless of the number of grooves on the cylinder surface.

Therefore, there is no difference in the flow structures among the stationary cases. As it is expected, the rotation of cylinders has a significant effect on the streamlines pattern inside the enclosure. It is shown that four corner vortices form inside the enclosure as a result of the interaction between the shear-driven and buoyancy-driven zones.

For RS=500, it seems that the shear-driven flow is relatively stronger for Case 2 with a smooth cylinder in comparison to grooved cases. Among the grooved cases, the last case provides a weaker shear-driven zone as illustrated in Fig. 10. Increasing the non-dimensional rotating speed up to 1000 expands the shear-driven zone more and more and the buoyancy-driven zone shrinks for all under consideration cases. Due to this fact, the corner vortices become smaller and occupy less region at the four corners of the enclosure.

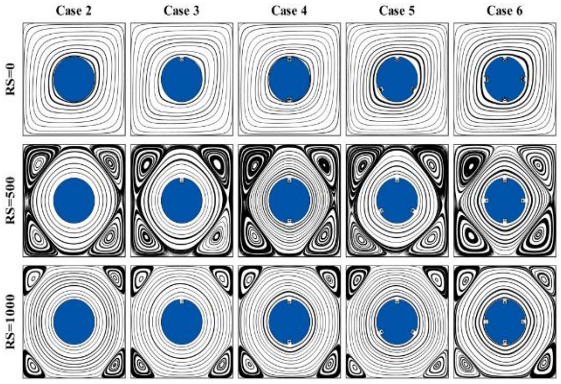

Fig. 10. Effect of rotating speed on the streamline patterns for R=0.2 and Ra=10^4

The effect of the non-dimensional rotating speed of the cylinder on the non-dimensional velocity magnitude distribution along the vertical line of x/L=-0.4 for Ra=10^4 and R=0.2 is presented in Fig. 11. As shown, under all considered non-dimensional rotating speeds of 100, 500, and 1000, the cylinder surface type affects the velocity distribution near the left wall although the difference among the cases is minimum for RS=100. At this non-dimensional rotating speed, at the half-lower side of the near-wall vertical line, the values of the velocity distribution are close to each other while at the half-upper side, Case 5 develops the maximum velocity gradient among all cases. Increasing the non-dimensional rotating speed up to 500 attenuates the velocity field near-wall region since the buoyancy-driven flow shows a tendency to become dominant around the cavity corners. As seen, three peak points can be observed for velocity magnitudes. Around the main peak point, Case 2 develops maximum velocity magnitudes due to a stronger shear-driven flow as discussed before. Beyond that, among the grooved cases, Case 6 and Case 4 develop maximum and minimum velocity gradients, respectively. Around the minor peaks, which are developed due to large-scale corner vortices, Case 6 forms the maximum velocity field, while Case 5 and Case 3 exhibit the minimum values on the left and right minor peaks, respectively. For RS=1000, in comparison to RS=500, the velocity field near-wall region augments gradually and the impact of the corner vortices on the velocity distribution minimizes. Except for points located inside the lower and upper corner vortices, Case 5 and Case 2 develop the maximum velocity field at half-lower and half-upper locations, respectively. Around the peak point, Case 2 exhibits the maximum velocity gradient due to the strongest shear-driven flow at this region as discussed before.

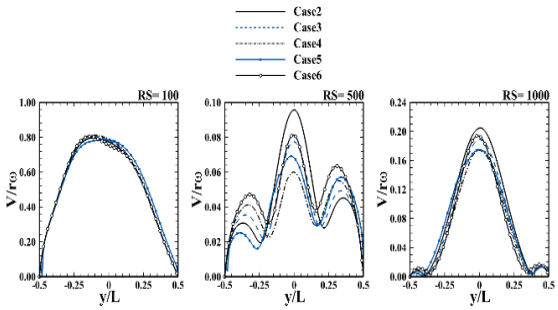

Fig. 11. Effect of rotating speed on the non-dimensional velocity magnitude at x/L=-0.4 for R=0.2 and Ra=10^4

Fig. 12 shows the distribution of non-dimensional temperature along the vertical line of x/L=-0.4 for Ra=10^4 and R=0.2. Under RS=100, as expected, using cylinders with different numbers of grooves slightly affects the distribution of non-dimensional temperature. Like the velocity distribution, the difference between the temperature distributions among the cases is minimum. In this rotating speed, since the dominancy of the rotating fluid zone is weaker in comparison to higher values of rotating speed, fluid is colder at the lower part of the considered line and is hotter at its higher locations. Increasing the non-dimensional rotating speed reveals the difference between the cases. Under RS=500 and 1000, because of the nature of vortical structures, corner vortices accelerate the mixing of the fluid. In this regard, near the upper and lower walls, where corner vortices are formed, the impact of mixing phenomena can be seen. Also, it is necessary to mention that the minimum peak occurred in curves under RS=500 and 1000 is due to the dominant rotating zone. In this line, it can be expected to have higher temperature gradients on the left wall near these minimum peak values of non-dimensional temperature. For RS=500 and 1000, except close to the peak point, Case 6 provides the minimum temperature gradient among all under consideration cases.

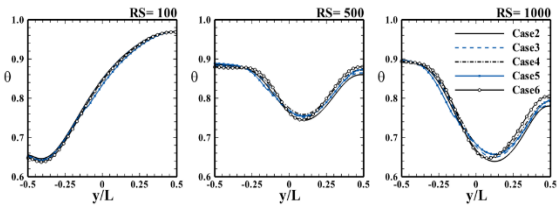

Fig. 12. Effect of rotating speed on the non-dimensional temperature at x/L=-0.4 for R=0.2 and Ra=10^4

5.3. Counterclockwise Rotation Versus Clockwise Rotation

The direction of rotation is another parameter, which is analyzed in the present study. Fig. 13 is presented to show the rotation direction impact on the flow structure inside the enclosure for Ra=10^4, R=0.2, and RS=0, 500, and -500. Since a clockwise rotating fluid flow naturally occurs in stationary conditions due to buoyancy effects, it can be expected that the clockwise rotation of the cylinder motivates further buoyancy-driven flow within the enclosure. This is completely in line with the obtained results for RS=-500. In this case, the number of grooves on the cylinder does not affect the flow structure inside the enclosure. In return, in counterclockwise rotation, a counterclockwise rotating zone is observed around the cylinder, which is because of the no-slip condition on the surface of the cylinder and viscous effects of the fluid, and four clockwise vortical structures are observed at the corners. Further examination of the flow structure inside the enclosure shows that the shape of the shear flow changes as a function of the groove number on the cylinder for RS=500. That is, the extension of shear flow inside the enclosure is almost along the grooves. In other words, for Case 3, Case 4, Case 5, and Case 6, the shear flow extension occurs in one, two, three, and four directions, respectively. However, for Case 2 (smooth cylinder case), a nearly circular fluid rotating zone is observed as illustrated in Fig. 13. Hence, it can be predicted that the occupied regions by corner vortices increase gradually as a function of the groove number for the counterclockwise rotating scenario.

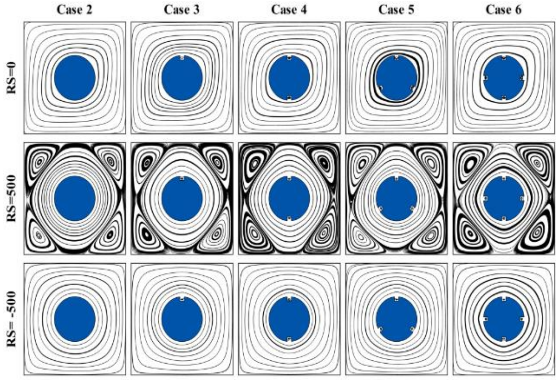

Fig. 13. Counterclockwise versus clockwise rotation effect on the streamline patterns for R=0.2 and Ra=10^4

To assess the computed results for the effect of rotation direction on the near-wall (x/L=-0.4) non-dimensional velocity distribution, Fig. 14 is presented for Ra=10^4, R=0.2, and RS= 500 and -500. As it is obvious, the direction of rotation plays an important role in fluid flow behavior inside the enclosure. For a clockwise rotating scenario, namely RS=-500, regardless of the surface type of the cylinder, rotating the cylinder enhances the momentum transfer near-wall region. In this case, except around the peak point, the velocity gradient is minimum and maximum at the half-lower side near the left wall for Case 6 and Case 5, respectively. At the half-upper side

near the left wall, the minimum and maximum velocity magnitudes occur for Case 6 and Case 4, respectively. Around the peak location, Case 2 having the strongest shear-driven fluid rotating zone provides the maximum velocity field as demonstrated in Fig. 14. For the counterclockwise rotating scenario, due to an interaction between the clockwise buoyancy-driven flow and counterclockwise shear-driven flow, the velocity field attenuates the near-wall region. Additionally, on the minor peaks resulting from corner vortices, the last case develops maximum velocity magnitudes whereas, on the main peak, Case 2 has the maximum velocity gradient.

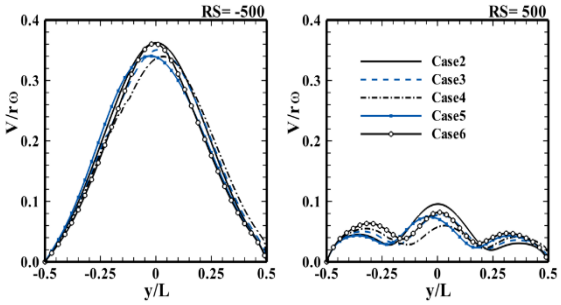

Fig. 14. Counterclockwise versus clockwise rotation effect on the non-dimensional velocity magnitude at x/L=-0.4 for R=0.2 and Ra=10^4

Fig. 15 shows the distribution of near-wall non-dimensional temperature of various cases with rotating cylinders under Ra=10^4 and R=0.2 along the vertical line of x/L=-0.4 for RS=-500 and 500. In line with previous discussions, a comparison of non-dimensional temperature distribution between clockwise and counterclockwise rotation near the right wall illustrates that clockwise rotation leads to gaining a wider range of variation. For all cases under RS=-500, due to accelerating the buoyancy-driven flow, at the lower part of the under consideration vertical line, the temperature is lower compared to the upper positions. However, under RS=500, as a result of corner vortex formation and consequently temperature mixing in these circulating regions, a slight difference is captured for the lower and upper parts of the vertical line. Additionally, it can be figured that under counterclockwise rotation, peak values of non-dimensional temperature curves occur because of the matter that rotating fluid contains higher non-dimensional temperature.

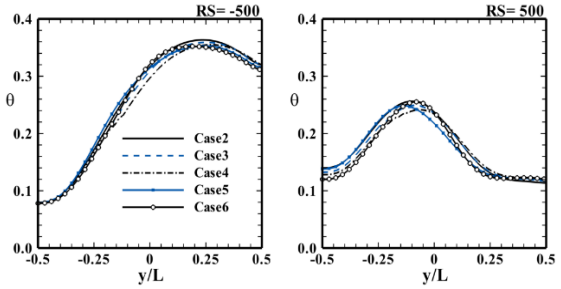

Fig. 15. Counterclockwise versus clockwise rotation effect on the non-dimensional temperature at x/L=-0.4 for R=0.2 and Ra=10^4

5.4. Effects of Rayleigh Number

Rayleigh number represents the ratio of buoyancy force to viscous forces. Therefore, higher values of Rayleigh number lead to stronger buoyancy forces. Fig. 16 is prepared to indicate the impact of Rayleigh number on the streamlines pattern under RS=100 and R=0.2. Initially, it is obvious that the Rayleigh number directly affects the both rotating fluid zone and vortical structures of fluid flow. Under Ra=10^3, a rotating fluid zone resulting from the shear-driven flow is captured around the cylinder. In this Rayleigh number, the shear-driven flow is strong and occupies a considerable region inside the enclosure. Hence, the weak buoyancy effects are observed as four vortical structures at four corners. The existence of grooves on the surface of a cylinder plays a key role in the formation of vortical structures and their sizes. Examination of the presented flow structures reveals that increasing the groove number attenuates and augments gradually the shear and buoyancy effects, respectively. Therefore, the corner vortices expand gradually as a function of the groove number. Increasing the Rayleigh number up to Ra=10^4 enhances the buoyancy effects and consequently, the shear-driven zone shrinks around the cylinder regardless of the groove number. In this situation, four distinguishable vortices can be realized on the upper and lower shoulders of each cylinder. The size of these vortical structures changes as a function of groove number. Further increasing the Rayleigh number up to Ra=10^5 augments the buoyancy effects inside the enclosure and hence, at both left and right sides of the cylinders, the vortical structures merge with each other, generally. As demonstrated, except in Case 6 with four well-known vortices, around the cylinders, a pair of vortical structures can be seen.

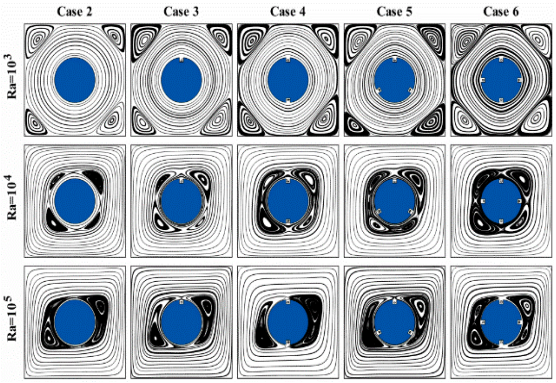

Fig. 16. Effect of Rayleigh number on the streamline patterns for R=0.2, RS=100

Fig. 17 illustrates the non-dimensional velocity magnitude distribution along the vertical line of x/L=-0.4 under RS=100 and R=0.2. As mentioned before, an increase in the Rayleigh number leads to a stronger buoyancy effect. The variation ranges of obtained results are precisely in line with this statement. As it seems, under $Ra=10^3$ corner vortices near the lower and upper walls affect the velocity magnitude curves, and the strongest vortices are being formed for Case 6. Except close to the insulated walls, the momentum transfer accelerates for Case 5 more than the other cases at -0.25<y/L<-0.1, and after that, among all cases, Case 2 exhibits the maximum momentum transfer. With increasing the Rayleigh number up to 10^4, a gradual augmentation in the velocity field near-wall region becomes obvious, the difference among the cases in general and at the half-lower location in particular reduces, and the effect of corner vortices eliminates. This occurrence continues for $Ra=10^5$ while a jump in the point-to-point velocity magnitudes near-wall region is felt. For both $Ra=10^4$ and 10^5, Case 4 develops a relatively higher velocity field at the half-upper position among the cases as illustrated in Fig. 17.

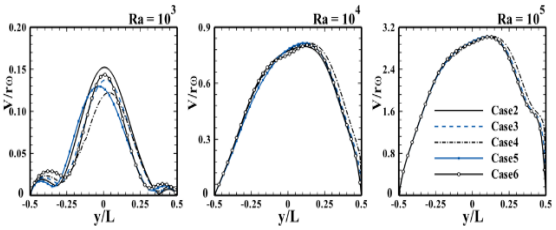

Fig. 17. Effect of Rayleigh number on the non-dimensional velocity magnitude at x/L=-0.4 for R=0.2, RS=100

The distribution of non-dimensional temperature along the vertical line of x/L=-0.4 under RS=100 and R=0.2 is indicated in Fig. 18. Due to the acceleration of the buoyancy-driven flow with an increase in the Rayleigh number, it can be observed that non-dimensional temperature varies in a wider range in a higher Rayleigh number. Under $Ra=10^3$, the shear-driven flow overcomes the buoyancy-driven flow near-wall region. For this, the values of the non-dimensional temperature at the half-lower side are higher compared with the half-upper position regardless of the groove number. In this situation, the temperature gradient is maximum and minimum respectively for Case 6 and Case 2 at the half-lower side, and at upper locations, Case 6 and Case 4 provide the maximum and minimum temperature gradients near-wall regions, respectively. With an increase in the Rayleigh number up to 10^4, the scenario reverses. That is, the buoyancy-driven flow dominates near-wall regions and hence, the non-dimensional temperature field varies from the lower side toward the upper side for all cases. In this Rayleigh number, for most locations near-wall regions, Case 6 and Case 4 exhibit maximum and minimum values, respectively. This event can be understood with consideration of the velocity magnitudes developed by cases near-wall region as presented in Fig. 17 and discussed in detail. Finally, at $Ra=10^5$, the difference between the cases minimizes as demonstrated in Fig. 18, and it can be stated that the buoyancy effect is the main player inside the enclosure.

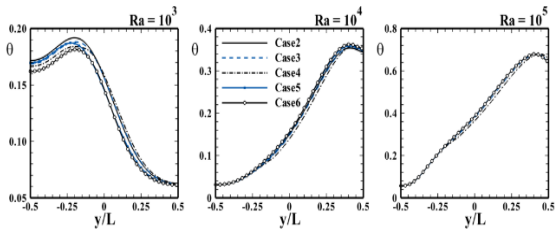

Fig. 18. Effect of Rayleigh number on the non-dimensional temperature at x/L=-0.4 for R=0.2, RS=100, and $Ra=10^4$

5.5. Thermal Performance

In this subsection, the thermal performance of all under consideration cases is discussed briefly. Fig. 19 (a)-(c) indicate the variations of average Nusselt number over the vertical walls for Cases 2-6 with respect to reference case as a function of all studied parameters. In Fig. 19 (a), the results are presented for $Ra=10^3$ as a function of R and RS. As it seems, the presence of a rotating cylinder can affect thermal performance both positively and negatively. In general, regardless of the radius ratio, the clockwise rotation of the cylinders enhances the rate of heat transfer inside the enclosure more than the counterclockwise rotation. For a minimum radius ratio of 0.1, the maximum heat transfer rate occurs for RS=-1000 and the minimum values are for RS=100. In the case of stationary cylinders, the values of the average Nusselt number, more or less, are identical to the reference case. For clockwise rotating cases, the rate of heat transfer varies as a function of RS, and to have a higher

relative Nusselt number than one for counterclockwise rotating cases, higher RS values are expected. On the other hand, for this minimum radius ratio under consideration, the difference among the cases is minimum under both clockwise and counterclockwise rotating scenarios due to the low shear-driven effects. At larger radius ratios such as 0.2 and 0.3, the difference among the cases becomes evident. In the other words, except for stationary cases, which exhibit a relative Nusselt number of less than one, among the rotating cases, the minimum and maximum heat transfer enhancements occur for RS=100 and RS=-1000, respectively. At each effective rotating speed, Case 2 (the case with a smooth cylinder) provides the maximum heat transfer rate and among the grooved cases, Case 5 (the case with three grooves) develops the maximum value. On the other hand, with increasing the radius ratio at this Rayleigh number, it seems the effects of rotation direction minimizes as can be clearly understood for R=0.3. Increasing the Rayleigh number up to $Ra=10^4$ increases the buoyancy-driven effects inside the enclosure as discussed before in detail. In this situation, despite $Ra=10^3$, the higher counterclockwise rotation has negative effects on the heat transfer rate inside the enclosure and only the clockwise rotation has positive effects in this regard for R=0.1. In a case with R=0.2, the minimum and maximum positive effects on the heat transfer rate can be reported for RS=-100 and RS=-1000 as demonstrated in Fig. 19 (b). For a maximum radius ratio of 0.3 at which the shear-driven effects are maximum for both clockwise and counterclockwise rotations, except RS=0 and 100, rotating the cylinder inside the enclosure has a positive effect on the heat transfer process. However, the maximum heat transfer rate occurs for Case 2 under RS=-1000, and among the grooved cased, Case 5 exhibits the maximum value. For a maximum Rayleigh number under consideration, as illustrated in Fig. 19 (c), the effects of the non-dimensional rotating speeds minimize. In this Rayleigh number, under R=0.1, only stationary, RS=-100, and RS=100 have positive effects on the heat transfer process inside the enclosure. For the other clockwise and counterclockwise rotating cases, the rate of heat transfer becomes less than that of the reference case. This occurrence, more or less, continues for R=0.2, and for R=0.3, and only RS=-1000 provides the relative average Nusselt number more than one with a similar variation like $Ra=10^3$ and 10^4.

In general, it can be understood that increasing the Rayleigh number reduces the enhancement of thermal performance in comparison with the reference case. It means that in order to have higher positive effects on the heat transfer inside the enclosure for larger Rayleigh numbers, higher rotating speeds require. In contrast with that, an increase in radius ratio positively affects the thermal performance of the enclosure. Additionally, the thermal performance of the enclosure under the stationary condition is not sensitive to the number of grooves on the surface of the cylinder. However, for all effective cases, the smooth cylinder and among the grooved cases, Case 5 provide the maximum thermal performances.

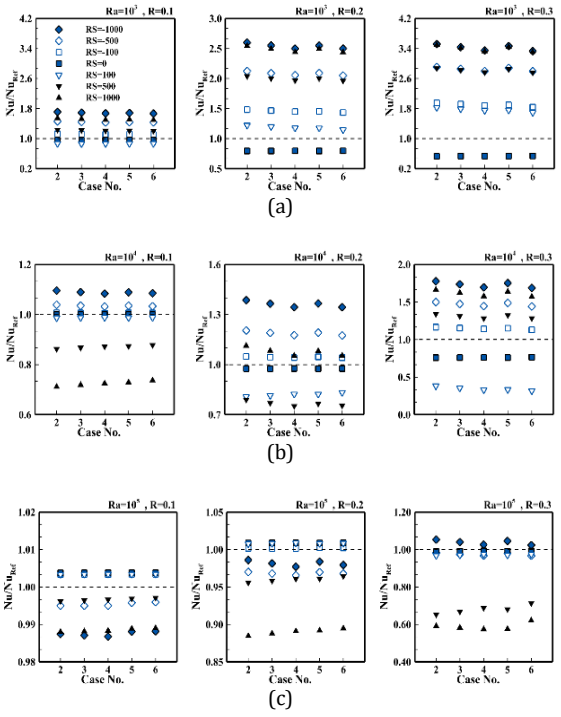

Fig. 19. Variations of thermal performance for all under consideration cases as a function of R, RS, and Ra

6. Conclusions

The convective heat transfer phenomenon inside an enclosure in the presence of a rotating groove cylinder was studied using a number of computations. Effects of groove number on the cylinder, rotation direction, rotating speed, radius ratio, and Rayleigh number were considered in this numerical research. Many different quantitative and qualitative results were presented and discussed to reveal the impacts of under consideration parameters. The obtained results were validated successfully against the available data for an empty enclosure and also for an enclosure containing a rotating smooth cylinder. The obtained results revealed that the existence of grooves on the cylinder has a considerable influence on the heat and fluid flow inside the enclosure. It was found that at small and moderate Rayleigh numbers, heat transfer inside the enclosure enhances with respect to the reference case as the radius ratio and rotating speed increase. However, for a specific rotating speed, clockwise rotating

provides a higher heat transfer rate compared with the counterclockwise scenario regardless of the groove number on the cylinder. At the large Rayleigh number, the impacts of radius ratio, rotating speed, and rotation direction attenuate dramatically. Finally, it was concluded that among all cases, Case 2 with 251.6% and among the grooved cases, Case 5 with 249.6% develop maximum heat transfer enhancements inside the enclosure. These maximum heat transfer enhancements occur for $Ra=10^3$, R=0.3, and RS=-1000.

Nomenclature

Symbol	*Description*
d	*Diameter of cylinder (m)*
g	*Gravitational acceleration (m/s²)*
L	*Width and height of enclosure (m)*
Nu	*Average Nusselt number*
p	*Pressure (Pa)*
Pr	*Prandtl number*
r	*Radius of cylinder (m)*
R	*Radius ratio*
Ra	*Rayleigh number*
RS	*Non-dimensional rotating speed*
T	*Temperature (°C)*
u	*Horizontal velocity component (m/s)*
v	*Vertical velocity component (m/s)*
V	*Velocity magnitude (m/s)*
V^*	*Non-dimensional velocity magnitude*
x	*Horizontal coordinate (m)*
y	*Vertical coordinate (m)*
Greek symbols	
α	*Thermal diffusivity (m²/s)*
β	*Thermal expansion coefficient (1/K)*
φ	*Polar angle*
θ	*Non-dimensional temperature*
ϑ	*Kinematic viscosity (m²/s)*
ρ	*Density (kg/m³)*
ω	*Rotating speed (rad/s)*
ξ	*Grid element size (m)*
Subscripts	
C	*Cold Wall*
H	*Hot wall*
Ref	*Reference*

Funding Statement

This research did not receive any specific grant from funding agencies in the public, commercial, or not-for-profit sectors.

Conflicts of Interest

The authors declare that there is no conflict of interest regarding the publication of this article.

References

[1] Selimefendigil, F. and Öztop, H.F., 2020. Mixed convection in a PCM filled cavity under the influence of a rotating cylinder. *Solar Energy*, 200, p. 61-75.

[2] Raizah, Z. and Aly, A.M., 2021. Double-diffusive convection of a rotating circular cylinder in a porous cavity suspended by nano-encapsulated phase change materials. *Case Studies in Thermal Engineering*, 24, p. 100864.

[3] Ghalambaz, M., et al., 2022. Unsteady natural convection of nano-encapsulated phase change materials (NEPCMs) inside a random porous medium considering local thermal non-equilibrium condition. *Waves in Random and Complex Media,* p. 1-22.

[4] Hussain, S., Alsedias, N. and Aly, A.M., 2022. Natural convection of a water-based suspension containing nano-encapsulated phase change material in a porous grooved cavity. *Journal of Energy Storage*, 51, p. 104589.

[5] Ouri, H., et al., 2022. *MHD* hybrid nanofluid convection and phase change process in an L-shaped vented cavity equipped with an inner rotating cylinder and PCM-packed bed system. *Alexandria Engineering Journal*, 2022.

[6] Qasem, N.A.A., et al., 2022. Effect of a rotating cylinder on convective flow, heat and entropy production of a 3D wavy enclosure filled by a phase change material. *Applied Thermal Engineering,* 214, p. 118818.

[7] Sadr, A.N., et al., 2022. Simulation of mixed-convection of water and nano-encapsulated phase change material inside a square cavity with a rotating hot cylinder. *Journal of Energy Storage*, 47, p. 103606.

[8] Ouri, H., et al., 2023. MHD hybrid nanofluid convection and phase change process in an L-shaped vented cavity equipped with an inner rotating cylinder and PCM-packed bed system. *Alexandria Engineering Journal*, 63, p. 563-582.

[9] Khanafer, K., Aithal, S.M. and Vafai, K., 2019. Mixed convection heat transfer in a differentially heated cavity with two rotating cylinders. *International Journal of Thermal Sciences*, 135, p. 117-132.

[10] Hassanzadeh, R., et al., 2020. Analysis of natural convection in a square cavity in the presence of a rotating cylinder with a specific number of roughness components. *International Communications in Heat and Mass Transfer,* 116, p. 104708.

[11] Pirmohammadi, M. and A. Salehi-Shabestari, 2020. Parametric Study of Natural Convection inside a Partitioned Cavity in the Presence of a Magnetic Field. *Journal of Engineering Physics and Thermophysics*, 93(5), p. 1255-1265.

[12] Hassen, W., et al., 2021. Control of Magnetohydrodynamic Mixed Convection and Entropy Generation in a Porous Cavity by Using Double Rotating Cylinders and Curved Partition. *ACS Omega*, 6(51), p. 35607-35618.

[13] Turkyilmazoglu, M., 2022. Exponential nonuniform wall heating of a square cavity and natural convection. *Chinese Journal of Physics*, 77, p. 2122-2135.

[14] Kardgar, A., 2023. Natural Convection and Entropy Generation of Non-Newtonian Hybrid Cu-Al2O3/Water Nanofluid in an Inclined Partial Porous Cavity with Different Local Heater Positions in the Presence of Magnetic Field. *Journal of Heat and Mass Transfer Research,* 2023. 10(2), p. 279-300.

[15] Mahmoodi, M. and Hemmat Esfe, M., 2015. Buoyancy driven heat transfer of a nanofluid in a differentially heated square cavity under effect of an adiabatic square baffle. *Journal of Heat and Mass Transfer Research,* 2(2), p. 1-13.

[16] Hemmat Esfe, M. and Saedodin, S., 2018. Numerical study of a combined convection flow in a cavity filled with nanofluid considering effects of diameter of nanoparticles and cavity inclination angles. *Journal of Heat and Mass Transfer Research,* 5(1), p. 39-49.

[17] Hassanzadeh, R., Rahimi, R. and Pekel, H., 2021. Effects of Shell Aspect Ratio and Combustion Chamber Location on Thermal–Hydraulic Performance of Hot-Water Steel Boilers Under Steady-State Operation. *Arabian Journal for Science and Engineering*, 46.

[18] Mohebbi, R., et al., 2021. Natural Convection Heat Transfer of Ag-MgO/Water Micropolar Hybrid Nanofluid inside an F-shaped Cavity Equipped by Hot Obstacle. *Journal of Heat and Mass Transfer Research*, 8(2), p. 139-150.

[19] El hamma, M., et al., 2023. Analysis of MHD Thermosolutal Convection in a Porous Cylindrical Cavity Filled with a Casson Nanofluid, Considering Soret and Dufour Effects. *Journal of Heat and Mass Transfer Research*, 10(2), p. 197-206.

[20] Shewale, V.C., Kapse, A.A. and Mogal, S.P., 2023. Analysis of Cylindrical Cavity Receiver for Different Heat Losses. *Journal of Heat and Mass Transfer Research*, 10(1), p. 43-50.

[21] Barnoon, P., et al., 2019. MHD mixed convection and entropy generation in a lid-driven cavity with rotating cylinders filled by a nanofluid using two phase mixture model. *Journal of Magnetism and Magnetic Materials*, 483, p. 224-248.

[22] Moayedi, H., Amanifard, N. and Deylami, H.M., 2022. A comparative study of the effect of fin shape on mixed convection heat transfer in a lid-driven square cavity. *Journal of the Brazilian Society of Mechanical Sciences and Engineering*, 44(8), p. 322.

[23] Triveni, M.K. and Panua, R., 2021. Natural and Mixed Convection Study of Isothermally Heated Cylinder in a Lid-Driven Square Enclosure Filled with Nanofluid. *Arabian Journal for Science and Engineering*, 46(3), p. 2505-2525.

[24] Tahmasbi, M., et al., 2020. Mixed convection enhancement by using optimized porous media and nanofluid in a cavity with two rotating cylinders. *Journal of Thermal Analysis and Calorimetry*, 141(5), p. 1829-1846.

[25] Aly, A.M., Raizah, Z.A.S., and Ahmed, S.E., 2021. ISPH simulations of natural convection from rotating circular cylinders inside a horizontal wavy cavity filled with a nanofluid and saturated by a heterogeneous porous medium. *The European Physical Journal Special Topics*, 230(5), p. 1173-1183.

[26] Dogonchi, A.S., et al., 2021. Thermal and entropy analyses on buoyancy-driven flow of nanofluid inside a porous enclosure with two square cylinders: Finite element method. *Case Studies in Thermal Engineering*, 27, p. 101298.

[27] Jabbar, M.Y., et al., 2021. Thermal analysis of nanofluid saturated in inclined porous cavity cooled by rotating active cylinder subjected to convective condition. *Journal of Thermal Analysis and Calorimetry*, 144(4), p. 1299-1323.

[28] Afroz, F. and Sharif, M.A.R., 2022. Numerical study of cross-flow around a circular cylinder with differently shaped span-wise surface grooves at low Reynolds number. *European Journal of Mechanics - B/Fluids*, 91, p. 203-218.

[29] Caliskan, M., et al., 2021. Investigation of flow characteristics for triangular grooved shape cylinder at different heights in shallow water. *Ocean Engineering,* 225, p. 108788.

[30] Farrokhi Derakhshandeh, J. and Gharib, N., 2020. Laminar flow instabilities of a grooved circular cylinder. *Journal of the Brazilian Society of Mechanical Sciences*, 42.

[31] Farrokhi Derakhshandeh, J., Ghorbani Tari, Z. and Gharib, N., 2021. Thermo-Fluids effects of a grooved circular cylinder in laminar flow regimes. *International Communications in Heat and Mass Transfer*, 124.

[32] Fujisawa, N., Hirabayashi, K. and Yamagata, T., 2020. Aerodynamic noise reduction of circular cylinder by longitudinal grooves. *Journal of Wind Engineering and Industrial Aerodynamics*, 199, p. 104129.

[33] Ozalp, C., et al., 2021. Heat transfer and flow structure around a heated cylinder by upstream installation of a grooved cylinder. *Experimental Thermal and Fluid Science*, 128, p. 110448.

[34] Song, X., et al., 2019. Application and optimization of drag reduction characteristics on the flow around a partial grooved cylinder by using the response surface method. *Engineering Applications of Computational Fluid Mechanics*, 13(1), p. 158-176.

[35] Wang, J., et al., 2019. Aerodynamic performance of a grooved cylinder in flow conditions encountered by bridge stay cables in service. *Journal of Wind Engineering and Industrial Aerodynamics*, 188, p. 80-89.

[36] Derakhhsandeh, J.F., Ghorbani Tari, Z. and Gharib, N., 2021. Thermo-fluids effects of a grooved circular cylinder in laminar flow regimes. *International Communications in Heat and Mass Transfer*, 124, p. 105272.

[37] Patankar, S., 2018. *Numerical heat transfer and fluid flow*. Taylor & Francis.

[38] Roslan, R., Saleh, H. and Hashim, I., 2012. Effect of rotating cylinder on heat transfer in a square enclosure filled with nanofluids. *International Journal of Heat and Mass Transfer*, 55(23), p. 7247-7256.

[39] Khanafer, K., Vafai, K. and Lightstone, M., 2003. Buoyancy-driven heat transfer enhancement in a two-dimensional enclosure utilizing nanofluids. *International Journal of Heat and Mass Transfer*, 46(19), p. 3639-3653.

[40] Ho, C.J., Chen, M.W. and Li, Z.W., 2008. Numerical simulation of natural convection of nanofluid in a square enclosure: Effects due to uncertainties of viscosity and thermal conductivity. *International Journal of Heat and Mass Transfer*, 51(17), p. 4506-4516.